

AD-A191 914

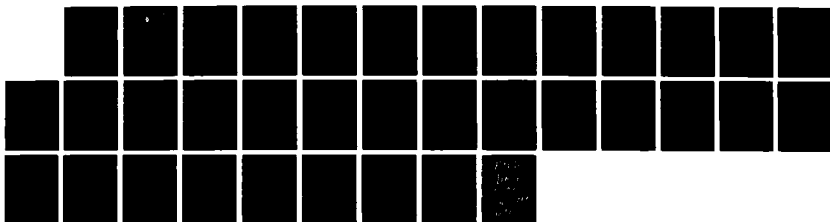
THE RELATIONSHIP BETWEEN APPENDAGE GEOMETRY AND
PROPELLER BLADE UNSTEADY FORCES(U) NAVAL OCEAN SYSTEMS
CENTER SAN DIEGO CA T S MAUTNER NOV 87

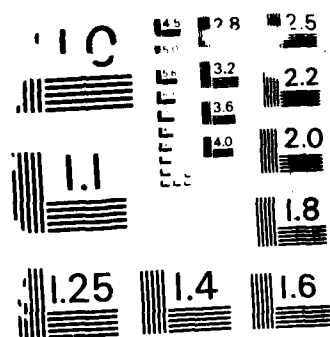
1/1

UNCLASSIFIED

F/G 13/10

NL





COPIES RESOLUTION TEST CHART
NATIONAL BUREAU OF STANDARDS-1963-A

AD-A191 914

①

UNCLASSIFIED
SECURITY CLASSIFICATION OF THIS PAGE

DTIC FILE COPY

DTIC REPORT DOCUMENTATION PAGE				
1a REPORT SECURITY CLASSIFICATION UNCLASSIFIED		1b RESTRICTIVE MARKINGS		
2a SECURITY CLASSIFICATION AUTHORITY S MAR 22 1988		3 DISTRIBUTION/AVAILABILITY OF REPORT Approved for public release; distribution is unlimited.		
2b DECLASSIFICATION/DOWNGRADING THE TITLE ca D		5 MONITORING ORGANIZATION REPORT NUMBER(S)		
4 PERFORMING ORGANIZATION REPORT NUMBER(S)		5 MONITORING ORGANIZATION REPORT NUMBER(S)		
6a NAME OF PERFORMING ORGANIZATION Naval Ocean Systems Center		6b OFFICE SYMBOL (if applicable) NOSC		7a NAME OF MONITORING ORGANIZATION Naval Ocean Systems Center
6c ADDRESS (City, State and ZIP Code) San Diego, CA 92152-5000		7b ADDRESS (City, State and ZIP Code) San Diego, CA 92152-5000		
8a NAME OF FUNDING SPONSORING ORGANIZATION Naval Underwater Systems Command		8b OFFICE SYMBOL (if applicable) NUSC		9 PROCUREMENT INSTRUMENT IDENTIFICATION NUMBER
8c ADDRESS (City, State and ZIP Code) Newport, RI 02841		10 SOURCE OF FUNDING NUMBERS		
		PROGRAM ELEMENT NO 62633N	PROJECT NO HM35	TASK NO SF33321
		AGENCY ACCESSION NO DN305 123		
11 TITLE (include Security Classification) The Relationship Between Appendage Geometry and Propeller Blade Unsteady Forces				
12 PERSONAL AUTHOR(S) T.S. Mautner				
13a TYPE OF REPORT Professional Paper		13b TIME COVERED FROM June 1987 TO July 1987		14 DATE OF REPORT (Year, Month, Day) November 1987
15 PAGE COUNT				
16 SUPPLEMENTARY NOTATION				
17 COSATI CODES			18 SUBJECT TERMS (Continue on reverse if necessary and identify by block number)	
FIELD	GROUP	SUB-GROUP	blade forces	
			incident velocity field distribution	
			propeller geometry	
19 ABSTRACT (Continue on reverse if necessary and identify by block number)				
<p>A study was undertaken to determine the relationship between appendage geometry, unsteady propeller blade forces and the incident velocity field distribution. Axial velocity data from water tunnel tests of an axisymmetric body with appendages has been used to calculate the harmonic content of the wake and the resulting distribution of unsteady thrust and torque for a given propeller geometry. The results indicate that unsteady force reduction can be obtained by modification of the flow at the appendage/body intersection, and by modification of the wake such that flow regions having substantial harmonic content lie outside the propeller's maximum diameter.</p>				
20 DISTRIBUTION/AVAILABILITY OF ABSTRACT <input type="checkbox"/> UNCLASSIFIED UNLIMITED <input checked="" type="checkbox"/> SAME AS RPT <input type="checkbox"/> DTIC USERS			21 ABSTRACT SECURITY CLASSIFICATION UNCLASSIFIED	
22a NAME OF RESPONSIBLE INDIVIDUAL T.S. Mautner			22b TELEPHONE (include Area Code) 619-225-2497	22c OFFICE SYMBOL Code 634

DD FORM 1473, 84 JAN

83 APR EDITION MAY BE USED UNTIL EXHAUSTED
ALL OTHER EDITIONS ARE OBSOLETEUNCLASSIFIED
SECURITY CLASSIFICATION OF THIS PAGE

AIAA'87

AIAA-87-2064

**The Relationship Between
Appendage Geometry and
Propeller Blade Unsteady Forces**

T.S. Mautner

Naval Ocean Systems Center
San Diego, CA

Accession For	
NTIS GRA&I	<input checked="" type="checkbox"/>
DTIC TAB	<input type="checkbox"/>
Unannounced	<input type="checkbox"/>
Justification	
By	
Distribution/	
Availability Codes	
st	Avail and/or Special

A-1



AIAA/SAE/ASME/ASEE 23rd Joint Propulsion Conference

June 29-July 2, 1987/San Diego, California

For permission to copy or republish, contact the American Institute of Aeronautics and Astronautics
1633 Broadway, New York, NY 10019

88 3 16 054

THE RELATIONSHIP BETWEEN APPENDAGE GEOMETRY AND PROPELLER BLADE UNSTEADY FORCES

T.S. Mautner
Hydromechanics Branch
Naval Ocean Systems Center
San Diego, CA 92152-5000

ABSTRACT

A study was undertaken to determine the relationship between appendage geometry, unsteady propeller blade forces and the incident velocity field distribution. Axial velocity data from water tunnel tests of an axisymmetric body with appendages has been used to calculate the harmonic content of the wake and the resulting distribution of unsteady thrust and torque for a given propeller geometry. The results indicate that unsteady force reduction can be obtained by modification of the flow at the appendage/body intersection, and by modification of the wake such that flow regions having substantial harmonic content lie outside the propeller's maximum diameter.

NOMENCLATURE

a_0	Zeroth order Fourier coefficient
a_n	n th order Fourier coefficient
b_n	n th order Fourier coefficient
B	Blade number
c_n	Complex Fourier coefficient = $a_n - ib_n$
C_n	Magnitude of the n th Fourier Coefficients
C_L	Blade section lift coefficient
C_T	Appendage chord at the tip
C_R	Appendage chord at the root
D_B	Body diameter
$F_x^{(m)}$	Unsteady axial force (thrust) for the m th harmonic
j	Index taking on values = 1, ..., P
k_{nj}	The reduced frequency, $\omega(C_j/2)/V_s$, at the j th element due to the n th harmonic of the inflow velocity
$K(k)$	Sear's function
K_T	Thrust coefficient = Thrust / $\frac{1}{2}\rho V_s^2 \pi R^2$

K_Q	Torque coefficient = $\text{Torque} / \frac{1}{2} \rho V_\infty^2 \pi R^3$
L_{jn}	Lift on the j th blade element due to the n th harmonic component of the inflow velocity
L_B	Body length
m	Order of the propeller force harmonic
M_{jn}	Moment/Torque on the j th blade element due to the n th harmonic component of the inflow velocity
n	Index taking on values = mB
nj	Identifies the j th blade element and n th harmonic component of the inflow velocity
N	Harmonic number
P	Number of blade elements having width Δr
PC	Propulsive coefficient = $(\text{Thrust} \cdot V_\infty) / (\text{Torque} \cdot \Omega)$
r	Radial coordinate
r_h	Hub radius
Δr_j	Width of the j th blade element
R	Propeller radius
R_B	Body radius
Re	Reynolds number based on body diameter
S_R	Slenderness ratio of an appendage = chord/thickness
t/C	Thickness-to-chord ratio
$T_x^{(m)}$	Unsteady moment (torque) for the m th harmonic
$T(k)$	Horlock's function
x	Longitudinal coordinate
X_o	Appendage axial offset
X_s	Streamwise location of the appendage leading edge
z	Distance from the body surface
Z_T	Radial location of the appendage tip
V	Velocity

V_s	Free stream velocity or vehicle speed
V_{rj}	Nondimensional, resultant relative velocity of blade section and fluid
Z_T	Appendage maximum radial position
α	Steady angle of attack of a blade element
β	Blade section pitch angle (radians)
ω	Frequency
Ω	Angular velocity of propeller
ψ	Phase shift
ρ	Fluid density
σ	Cavitation number based on free stream static pressure and velocity
θ	Angular coordinate

INTRODUCTION

A propeller operating in the turbulent wake of a torpedo or submarine encounters wake non-uniformities which result in spatial and temporal fluctuations of blade angle-of-attack. These angle-of-attack fluctuations result in unsteady blade loadings and the generation of noise. In addition to possible, direct radiation from a vibrating blade, the time-dependent forces on the propeller blade are transmitted as vibratory forces and moments through the propeller shafts and bearings to the vehicle's structure.¹ These unsteady forces may then result, for example, in the radiation of noise from the vehicle's shell and in the generation of vehicle self-noise. The sources of propulsor generated noise can be characterized by three types of unsteady force mechanisms: a) turbulence ingestion; b) vortex shedding; and c) blade-rate. The first two mechanisms typically generate continuous spectrum (broadband) radiated noise levels while blade-rate forces generate discrete frequency noise levels at various blade-passage frequencies and harmonics.

The flow nonuniformities which result in blade-rate propulsor noise are caused by

upstream appendages and their interaction with the hull boundary layer. The flow behind an appendage or appendage/stator combination is characterized by a complex velocity field having velocity excesses at the inner radii and velocity deficits at the outer radii (for example, see figure 4). This type of velocity field results in a complex harmonic content distribution where both the amplitude and phase vary with radial position. The effects of this varying inflow velocity field on blade-rate noise cannot be predicted without a detailed examination of the wake and calculations made for each radius and blade geometry. It should be remembered that the reduction of blade-rate noise was the original reason for the introduction of skew (a combination of blade warp and rake) into propeller design.

Currently, techniques are available for computing unsteady forces and skew distributions, and these methods range from low aspect ratio approximations to unsteady airfoil theory to complete unsteady, lifting-surface methods. Even though the NOSC designed counterrotating propellers have demonstrated exceptional hydrodynamic performance and good overall radiated noise characteristics, the results of at-sea tests indicate that research should be directed toward increased blade-rate noise reduction. Thus, the objective of the work described herein is to identify the contribution of the radial and circumferential nonuniformities in a wake to the unsteady force distribution on a propeller blade. The distribution of the wake nonuniformities and the calculated, radial distribution of propeller blade forces will be used to suggest improvements in appendage design.

MODEL GEOMETRY AND INFLOW VELOCITY FIELD

In the design of wake-adapted propellers, it is important that the inflow velocity distribution be properly specified. The state-of-the-art in boundary layer computations is such that the inflow velocity field, for a body having appendages located upstream of the propulsor, should be determined experimentally. Even though circumferentially averaged velocity profiles are sufficient for propeller design calculations, the calculation of unsteady blade forces requires that both the radial and circumferential distributions of the wake be considered.

The velocity fields used in this study were obtained from water tunnel tests conducted at Applied Research Laboratory of the Pennsylvania State University (ARL/PSU) (see Thompson, 1986). The tests were conducted in the closed-circuit, closed-jet water tunnel which has a 14 foot long 48 inch diameter test section. A flow correcting liner was installed in the test section to adjust the streamlines around the model to approximate the streamlines that would exist around the vehicle in open water operation. The model, torpedo like in shape, had a forshortened length-to-diameter ratio of $L_B/D_B=7.6$. Screens were wrapped around the model's forebody to assist in the generation of a full scale turbulent boundary layer in the afterbody region. The afterbody geometry is given in figure 1.

Three appendage configurations were used to obtain the velocity distribution used in this study. The general characteristics of the appendages are presented in table 1 and defined in figure 2. The appendages, designated fin 1, fin 2 and fin 3, are shown schematically in figure 3. A detailed description for fin 1 can be found in Nelson and Fogarty (1977) while Greeley and Milewski (1986) describe fins 2 and 3. Briefly, fins 1 and 2 have airfoil sections of constant thickness-to-chord from root to tip while fin 3 has an airfoil section thickness-to-chord ratio which decreases from the root to the tip. Also, fin 2 has a cap extending the length of the fin chord at the tip, and fin 3 has a "winglet" located in the aft region of the fin's tip chord (see the solid portions of figure 3).

For each appendage configuration, the axial, radial and tangential components of the velocity field were determined from 5-hole probe measurements. The velocity measurements were made at the propeller stacking line locations indicated in figure 1 where, behind each fin, 125 data points in the circumferential direction and 6 radial locations for fin 1 and 12 radial locations for fins 2 and 3 define the velocity field. The circumferential variation of the axial velocity components, $V(r,\theta)$, V_{θ} , for the three appendage configurations are shown in figures 4-6. For illustration purposes, the measured velocity at only six radial positions are shown for fins 2 and 3.

The polar plots presented in figures 4-6 were constructed using the axial velocity measured over the angular extent of $-45^\circ < \theta < +45^\circ$ where $\theta=0$ coincides with the fins trailing edge. Since

there are four identical fins, symmetry was used to obtain the 360° velocity field used in the Fourier analysis. The velocity data for all three fins exhibit the velocity excesses at the inner radii and the velocity deficits at the outer radii typically found in the flow behind an appendage on an axisymmetric body. The velocity excesses are due to the horseshoe vortex formed at the appendage/body intersection, and the velocity deficits at the outer radii are due to the fin's tip vortex (see Greeley and Milewski, 1986). The character of the velocity deficits for fins 2 and 3 are also influenced by the vorticity shed from the fin caps. This effect can be seen in velocity trace number 5 (figure 5) for fin 2 and in trace number 12 (figure 6) for fin 3 where the deficits are more broad in nature than that found for fin 1's velocity traces numbers 5 and 6.

FOURIER ANALYSIS

Unsteady forces are generated by both temporal and spatial variations of the velocity field; however, only the spatial variation of the inflow velocity field will be considered. The axial velocity data presented in figures 4-6 represents a time averaged, spatially varying field, and since the spatial velocity distribution is periodic and continuous, it may be represented by a Fourier series. For example, the axial component of the velocity at a position (r, θ) can be expressed as

$$\frac{V(r, \theta)}{V_s} = \frac{a_0(r)}{2} + \sum_{n=1}^{\infty} \left[a_n(r) \cos(n\theta) + b_n(r) \sin(n\theta) \right] = \text{Re} \left\{ \frac{a_0}{2} + \sum_{n=1}^{\infty} c_n e^{in\theta} \right\} \quad (1)$$

where $\text{Re}(\)$ denotes the real part, $c_n(r) = a_n(r) - i b_n(r)$ is a complex Fourier coefficient and $C_n(r) = (a_n^2(r) + b_n^2(r))^{1/2}$ is the Fourier coefficient magnitude. The Fourier coefficients, $a_0(r)$, $a_n(r)$ and $b_n(r)$, are defined by

$$a_0(r) = \frac{1}{\pi} \int_{-\pi}^{\pi} \frac{V}{V_s} d\theta \quad a_n(r) = \frac{1}{\pi} \int_{-\pi}^{\pi} \frac{V}{V_s} \cos(n\theta) d\theta \quad b_n(r) = \frac{1}{\pi} \int_{-\pi}^{\pi} \frac{V}{V_s} \sin(n\theta) d\theta \quad (2)$$

The term $a_0(r)$ does not vary in θ and, thus, is associated with the steady state thrust and torque. The additional terms are sinusoidal fluctuations of the inflow velocity which produce the unsteady forces and moments. A Fourier analysis of a four cycle wake (due to four appendages) would show that the

harmonics of interest are $N=4,8,12,16,\dots$. Additionally, it has been shown by Thompson (1976), that the only harmonic numbers of concern, in the calculation of unsteady forces and moments, are those associated with a multiple of a) blade number (mB), and b) blade number plus/minus one ($mB\pm 1$) which result in unsteady a) thrust and torque and b) side forces and moments respectively. Since the propeller configuration used in the calculations to follow is a 6 bladed propeller, the harmonic numbers of interest are $N=6,12,18,24,30,\dots$. Thus, for the case of the 6 bladed propeller in a 4 cycle wake, the first three harmonics of interest are $N=12, 24$, and 36. Fourier analysis of the wakes generated by fins 1, 2 and 3 yield the radial variation the harmonic coefficients shown in figures 7-9 for the dominant 12th harmonic.

Briefly, for $N=12$, the radial distribution of $a_n(r)$ for fins 1-3 show a large negative magnitude near the body surface ($r/R_B < 0.5$). For $r/R_B > 0.6$, a_n becomes positive and has a broad peak at the outer radii. In contrast, the $a_n(r)$ for fins 2 and 3 become positive but constant over mid-radii then have a large peak at the outer radii. The peak value occurs at approximately $r/R_B=0.8$ for fin 2 and $r/R_B=0.95$ for fin 3. The character of the harmonic distribution for $N=24$ shows that $a_n(r)$ has a peak at the same outer radii as $N=12$ but its magnitude is reduced by 50% or more. Finally for $N=36$, $a_n(r)$ has a nearly constant magnitude over radius. For all cases, $b_n(r)$ shows only small variations with radius and appendage type.

UNSTEADY FORCE CALCULATION METHOD

During the force calculation process, unsteady propeller blade forces will be calculated many times. Therefore, it would be desirable to use an efficient, inexpensive method. Some of the unsteady force calculation methods available are: 1) quasi-steady using uniform flow; 2) quasi-steady using lifting-line theory; 3) two-dimensional unsteady theory; and 4) three-dimensional unsteady theory. Quasi-steady methods use the instantaneous inflow velocity to solve the steady state problem while two-dimensional, unsteady methods do not include three-dimensional flow effects and ignore the influence of one blade section on another. Three-dimensional unsteady airfoil theory includes

three-dimensional flow effects and the interactions between blade sections. The theory adequately predicts the unsteady forces; however, it is computationally expensive.

The method chosen for the force calculations reported herein uses a two-dimensional approach developed by Thompson (1976). His theory divides the propeller blade into strips (blade elements of width Δr) which are treated as two-dimensional airfoils, and the method includes a correction to the lift due to the presence of other propeller blades. An integral part of Thompson's method is the theory developed by Sears and Horlock. Sears (1941) developed a two-dimensional, unsteady airfoil theory which accounts for sinusoidal gusts normal to the free stream velocity. Horlock (1968) extended Sears work to include sinusoidal velocity fluctuations parallel to the free stream velocity, and his analysis also allows the inclusion of general, sinusoidally varying inflow velocities. Recently, the two-dimensional, unsteady theory for cambered airfoils developed by Naumann and Yeh (1973) and the capability to calculate total forces and moments on the propeller were added to Thompson's method by Mautner and Blaisdell (1987).

Thompson (1976) has shown that only certain harmonics of the propeller's inflow velocity field contribute to the unsteady forces and moments. As stated above, the forces on a six bladed propeller operating in a four cycle wake are being calculated, thus only those harmonics which are integer multiples of the number of propeller blades need be considered. Therefore, the forces of interest are the unsteady thrust, $F_x^{(m)}$, and the unsteady torque, $T_x^{(m)}$ which are evaluated using the equations

$$F_x^{(m)} = B \left| \sum_{j=1}^P \left[L_{j(mB)} \right]_1 e^{-imB\psi_j} \right| \quad \text{and} \quad T_x^{(m)} = B \left| \sum_{j=1}^P \left[M_{j(mB)} \right]_1 e^{-imB\psi_j} \right| \quad (3)$$

where the unsteady forces due to the different harmonic groups fluctuate at the frequencies, $mB\Omega$. Equation (3) yields the total thrust and torque exerted on a propeller having B blades and P elements per blade. The lift and moment components used in the equation (3) are defined in equations (4) and

(5) below where the indices are $n=mB$ indicating the harmonic numbers and $j=1, \dots, P$ identifying the blade elements.

$$\left[L_{jn} \right]_1 = - \left[\frac{\partial C_L}{\partial \alpha} \right]_j \rho \frac{C_j}{2} V_{rj} V_{s, c_{nj}} \left\{ K(k_{nj}) \cos \beta_j - \alpha_j T(k_{nj}) \sin \beta_j \right\} \Delta r_j \cos \beta_j \quad (4)$$

$$\left[M_{jn} \right]_1 = \left[L_{jn} \right]_1 r_j \tan \beta_j \quad (5)$$

PROPELLER GEOMETRY

The investigation of the effect of harmonic content on the radial distribution of unsteady forces requires specification of propeller geometry and operating conditions. The geometry chosen is that for the forward propeller of a counterrotating propeller set designed using the method developed by Nelson (1972, 1975). The design utilized the circumferential mean, axial inflow velocity field measured by Nelson and Fogarty (1977). The propeller geometry is shown schematically in figure 10, and details of the propeller geometry and operating conditions are given in table 2. It should be noted that the wake used in the propeller design was obtained from wind tunnel tests; however, there is good agreement between the circumferential mean, axial velocity profiles obtained in the wind and water tunnel tests (using fin 1). While it would be more correct to design a propeller specifically for each appendage generated inflow, it is anticipated that only small changes in geometry would occur since the circumferential mean velocity profiles measured for fins 2 and 3 are nearly the same and are only slightly more "full" for $r/R_B < 0.75$. Therefore, it was decided to use the same geometry for all force calculations.

UNSTEADY FORCE CALCULATIONS

To determine the effect of each portion of the wake on the magnitude of the unsteady forces, the analysis included the following steps: a) modification of the measured, inflow velocity field by replacing the circumferentially varying velocity at a particular radial location by its circum-

ferential mean value; b) Fourier analysis of the modified wake; and c) calculation of the unsteady forces. It should be noted that forces will be used to indicate both thrust and torque.

The radial distribution of forces were calculated for harmonic numbers $N=12$, 24 and 36. The results for the dominant 12th harmonic are given in figures 11-13 for fins 1-3 respectively. The calculations show that the wakes generated by all three appendages result in large magnitude forces at the outer radii. The radial extent of these forces becomes more narrow as one changes from fin 1 ($0.6 < r/R_B < 0.9$) to fin 2 ($0.75 < r/R_B < 0.9$) and fin 3 ($0.85 < r/R_B < 1.0$). The results in figures 11-13 also show that the maximum force for fin 2 is approximately twice that found for either fin 1 or 3, and that the forces calculated for fins 2 and 3, at the inner radii, are lower in magnitude and more concentrated near the body surface than those found for fin 1. The radial distribution of forces calculated for $N=24$ show maximum forces at the same outer radial locations as found for $N=12$; however, the peak magnitudes are approximately 50% lower than those obtained for $N=12$. Additionally, the radial variation of forces for $N=36$ show a nearly constant magnitude over radius, and their magnitudes are, on the average, approximately 75% lower than the force magnitudes found for $N=12$.

The values of total thrust and torque calculated for harmonic numbers $N=12$, 24 and 36 are presented in tables 3-5 for fins 1-3 respectively. The results first list the forces calculated using the measured wake and then present the results of modifying the wake at one or more radial positions. For the measured wake, the forces obtained for all three fins show a reduction in magnitude with increasing harmonic number. As each one of the circumferentially varying velocity measurements was individually replaced by its circumferential mean value, the calculated forces (tables 3-5) show the expected result that elimination of a particular portion of the varying velocity field removes the contribution of that portion of the wake in the total force(s) magnitude. The degree of total thrust and torque reduction can be directly correlated to the peak forces found in the radial distributions (i.e the peak forces noted in figures 11-13 for $N=12$). It is also found that, in some cases, the reduction of the thrust and torque at one or more harmonics will in fact increase the magnitude of these forces at another harmonic. For example, for fin 3 the large reduction in thrust and torque at

$N=12$ ($\approx 75\%$) and 24 ($\approx 50\%$) due the modification of the wake at radial location number 10 results in a increase in the thrust and torque for $N=36$ of 2-2.5 times the magnitudes obtained for the measured wake.

Replacement of groups of radial locations with their circumferential mean values shows that elimination of the varying velocity at the inner radii does not produce an immediate benefit. This is due to the much larger magnitude forces found at the outer radii. However, the elimination of the spatial variations of the velocity field at the outer radii produces large changes in the total force magnitudes, especially for $N=12$, as shown by the data in tables 3-5 for locations 4-6 for fin 1 and locations 9-12 for fins 2 and 3. The results also show that the level of force reduction (increase for fin 3 at $N=36$) depends on both the appendage geometry and harmonic number, and that, in particular, appendages with shorter chord lengths (fins 2 and 3) generate wakes which result in lower overall unsteady force levels.

One implication of the radial force distributions given in figures 12 and 13 (peak forces near the maximum body diameter) is that reduced propeller unsteady forces can be obtained by keeping the propeller radius smaller than the radius at which the peak forces occur. The current NOSC design procedure is, after examining the input velocity distribution, to keep the propeller maximum radius smaller than the radial location of the appendage tip vortex; however, this was not done in this study in order to demonstrate the effect of the entire wake on the propeller forces. Also, the broad velocity deficits due to the vorticity shed from the tip cap (fin 2) and the "winglet" (fin 3) result in the peak forces noted in figures 12 and 13. Again, the propeller maximum radius should be kept smaller than the radial extent of this vorticity field.

APPENDAGE/BODY INTERACTION

The intersection of airfoils/hydrofoils/wings and plates/hulls/fuselages has been the subject of considerable research. For example, consider the work of Johnston (1960), Barber (1978) and Kubendran et al (1986). Johnston (1960) determined that the intersection of a cylinder with a plane

results in a three-dimensional stagnation point in front of the cylinder and the formation of a horseshoe vortex. Barber (1978) formulated a model describing the flow at the appendage/wall intersection for both thin and thick boundary layers. His model is reproduced in Figure 14. For a thick boundary layer, Barber's model indicates a stagnation point upstream of the appendage and the formation of a large horseshoe vortex near the leading edge of the appendage which spreads outward as it convects downstream. Barber also states that: a) the path of the horseshoe vortex is determined by the interaction of the onset boundary layer and the appendage pressure field; b) the strength of the vortex is dependent upon the edge velocity and the local boundary layer thickness; c) the size of the vortex will determine the flow field downstream; and d) the horseshoe vortex contribution is dominant in flows where the onset boundary layer is on the order of the appendage maximum thickness.

The more recent work of Kubendran et al (1986) presents the conclusion that the shape of the leading edge of the appendage is the major factor determining the entire flow field around the juncture. They also determined that the strength of the vortex is dependent upon the slenderness ratio, and, in general, the more blunt the leading edge the stronger the vortex. From their work, Kubendran et al suggested that the strength and location of the horseshoe vortex can be controlled by suitable modification of the leading edge shape.

The force calculation results presented in the previous section indicate that, at least for the current appendage geometries, there are two regions which should be considered in order to reduce propeller blade forces (in addition to the application of propeller blade warp and rake). First, the area associated with the vorticity shed at the appendage tip can be easily avoided by keeping the propeller maximum radius smaller than this region. The second area of concern is the flow field near the wall. As indicated in the above models, the appendage/body intersection will result in the generation of a horseshoe vortex which results in the type of velocity excesses present in the current velocity data.

Placing the current experimental data in the context of the models of Barber (1978) and Kubendran et al (1986) one can see that a strong horseshoe vortex will be formed at the

appendage/body intersection since the appendage is located in a boundary layer of thickness on the order of the appendage height (much greater than the maximum appendage thickness) and since the appendage geometries (i.e. the slenderness ratios $S_R = 8.3, 10$ and 5.9 for fins 1, 2 and 3 respectively) are appropriate for influencing the size and strength of the horseshoe vortex.

The current data shows that the characteristics of the velocity excess region changes with appendage geometry. By comparing figures 4 and 6 for fins 1 and 3, it can be seen that there is a reduction in the region of velocity excess, both in magnitude and radial extent, for fin 3. Also, the flow behind fin 3 is improved due to the smaller slenderness ratio of $S_R=5.9$ for fin 3 as compared to $S_R=8.3$ for fin 1. It should be noted that the airfoil sections used in fin 3 are more slender shape than the airfoil section of fin 1 thus reducing the adverse effect of a blunt leading edge. The current results also indicate that the unsteady forces due to the horseshoe vortex are also reduced due to a more favorable interaction of the onset flow and the appendage pressure gradient. This is shown (figures 4-6) by the smaller rate of spreading of the horseshoe vortex in both the radial and circumferential directions. Finally, fin 3 has a fillet-like base which produces a smooth transition of the appendage geometry to the body surface. This shape reduces the adverse effects of the sharp corners present at the intersection of, for example, fin 1 and the model's surface.

CONCLUSION

It can be concluded from the experimental data and the calculated unsteady forces that both the flow field near the body surface and behind the appendage tip must be considered in the process of reducing unsteady propeller blade forces. By keeping the propeller radius smaller than the appendage tip vortex region, the large magnitude forces generated by the tip vortex (with or without caps or "winglets") can be successfully avoided. However, an appropriate choice of appendage geometry must be made in order to reduce the effects of the horseshoe vortex formed at the appendage/body intersection. The significant change in geometry from fin 1 to fin 3 demonstrates the validity of the models presented by Johnston (1960), Barber (1976) and Kubendran et al (1986).

and the design of appendages should include consideration of the proposed methods of vortex size and strength reduction. Since the state-of-the-art in boundary layer calculations is such that these complex flow fields cannot be calculated easily, experiments are required to accurately determine the velocity field required in the prediction and reduction of propeller blade unsteady forces.

ACKNOWLEDGEMENTS

The work reported herein was funded in part by the Naval Ocean Systems Center's Internal Exploratory Development Program and the Torpedo Silencing Program administered by the Naval Underwater Systems Center. The author expresses his appreciation to W. Thompson, A. Treaster and W. Zierke of ARL/PSU for their extensive help during this project.

REFERENCES

- Barber, T.J., "An Investigation of Strut-Wall Intersection Losses," J. Aircraft, Vol 15, 1978, p 676.
- Greeley, D.S. and Milewski, W., "Hydrodynamic Design of Tail Fins for the NUSC WSRV," AARC Report No. 038, 1986.
- Horlock, J.H., "Fluctuating Lift Forces on Airfoils Moving Through Transverse and Chordwise Gusts," J. Basic Eng., Vol. 90, 1968, p 464.
- Johnson, J.P., "The Turbulent Boundary Layer at a Plane of Symmetry in a Three-Dimensional Flow," J. Basic Eng., Vol. 82, 1960, p 622.
- Kubendran, L.R., McMahon, H.M. and Hubbartt, J.E., "Turbulent Flow Around a Wing/Fuselage-Type Junction, AIAA J., Vol. 24, 1986, p 1447.
- Mautner, T.S. and Blaisdell, G.A., Author's Technical Notes Being Prepared For Publication, 1987.
- Naumann, H. and H. Yeh, "Lift and Pressure Fluctuations of a Cambered Airfoil Under Periodic Gusts and Applications in Turbomachinery," J. of Eng. and Power, Vol. 95, No. 1, 1973.
- Nelson, D.M. and Fogarty, J.J., Private Communication, 1977.
- Nelson, D.M., Development and Application of a Lifting Surface Design Method for Counterrotating Propellers, NUC TP 326, 1972.
- Nelson, D.M., A Computer Program Package for Designing Wake-Adapted Counterrotating Propellers: A User's Manual, NUC TP 494, 1975.

Sears, W.R., "Some Aspects of Non-Stationary Airfoil Theory and Its Practical Application," J. Aero. Sciences, Vol. 8, 1941, p 104.

Thompson, D.E., Propeller Time-Dependent Forces Due To Nonuniform Flow, ARL/PSU TM No. 76-48, 1976.

Thompson, D.E., Private Communication, 1986.

Table 1. Appendage Parameters

Fin #	C_R/D_B	C_T/D_B	$(t/C)_R$	$(t/C)_T$	X_o/D_B	Z_T/R_B	Re
Fin 1	0.76	0.76	0.12	0.12	0.0	0.994	4.3×10^4
Fin 2	0.40	0.34	0.10	0.10	0.06	0.943	5.5×10^4
Fin 3	0.49	0.29	0.17	0.11	0.19	0.948	5.5×10^4
Subscripts T = tip; R = root							

Table 2. Test Propeller Geometry and Operating Characteristics

Number of Blades	B	6
Propeller Radius (ft)	R	0.875
Hub Radius (ft)	r_h	0.287
Propeller Rotation	RPM	1400
Vehicle Speed (fps)	V_s	72.6
Cavitation Index	σ	0.9
Thrust Coefficient	K_T	0.108
Torque Coefficient	K_Q	0.059
Propulsive Coefficient	PC	0.87

r/R_B Radius	$\Delta r/R_B$ Strip Width	$\frac{1}{2}C$ Semi-Chord (ft)	β Pitch (rad)	V_{rj}/V_s Rel. Velocity
0.3447	0.0336	0.113145	0.576841	0.738605
0.3783	0.0336	0.121149	0.616340	0.843719
0.4119	0.0336	0.128814	0.645702	0.942810
0.4455	0.0336	0.136125	0.655345	1.031411
0.4791	0.0336	0.143065	0.658019	1.112655
0.5128	0.0336	0.149611	0.662808	1.190294
0.5464	0.0336	0.155739	0.666440	1.264405
0.5800	0.0336	0.161418	0.664828	1.335521
0.6136	0.0336	0.166610	0.657412	1.404553
0.6472	0.0336	0.171262	0.646083	1.472087
0.6808	0.0336	0.175304	0.633617	1.539381
0.7144	0.0336	0.178625	0.620620	1.606385
0.7480	0.0336	0.181013	0.606226	1.672096
0.7816	0.0336	0.181616	0.589710	1.735867
0.8152	0.0336	0.179654	0.570392	1.797638
0.8488	0.0336	0.173874	0.548253	1.858500
0.8824	0.0336	0.163055	0.523809	1.918692
0.9160	0.0336	0.146230	0.500699	1.978347
0.9496	0.0336	0.122573	0.482279	2.037898
0.9832	0.0336	0.091345	0.460723	2.097179

Table 3. Calculated Total, Unsteady Thrust and Torque for Fin 1.

Wake* Mod	N = 12		N = 24		N = 36	
	F **	T **	F	T	F	T
None	64.15	30.21	58.09	24.71	38.48	16.67
1	64.09	30.33	57.41	24.57	38.60	16.69
2	69.88	32.00	55.80	24.10	37.96	16.53
3	71.40	33.01	54.39	23.47	36.57	16.03
4	49.23	24.38	49.68	21.35	33.99	14.94
5	36.61	14.87	26.33	10.61	10.82	4.41
6	38.64	18.81	49.14	20.55	35.24	15.12
1-3	79.45	35.26	51.53	22.74	36.22	15.93
4-6	27.08	7.81	7.83	2.31	3.56	1.14
<p>Notes</p> <p>* The value(s) in this column refer to which radial location(s) of the wake was set to the circumferential mean value.</p> <p>** Units (F)orce (thrust) - pounds; (T)orque - foot pounds</p>						

Table 4. Calculated Total, Unsteady Thrust and Torque for Fin 2.

Wake* Mod	N=12		N=24		N=36	
	F **	T **	F	T	F	T
None	57.66	25.05	35.21	14.76	18.23	7.45
1	58.90	25.31	34.86	14.69	18.22	7.45
2	58.15	25.19	35.11	14.73	18.06	7.41
3	57.78	25.09	34.61	14.60	17.53	7.27
4	57.36	24.97	34.21	14.46	17.51	7.24
5	55.62	24.36	33.09	14.06	16.59	6.91
6	54.88	23.97	32.40	13.73	15.77	6.54
7	53.01	23.08	31.13	13.10	15.11	6.18
8	50.99	22.07	30.46	12.72	14.14	5.66
9	50.98	21.95	29.11	11.99	14.54	5.75
10	52.60	22.55	26.78	10.92	12.21	4.72
11	27.54	12.53	34.78	14.58	22.72	9.40
12	57.80	25.11	35.08	14.70	18.24	7.45
1-2	59.51	25.47	34.76	14.67	18.05	7.40
3-8	41.58	18.40	21.39	9.42	5.66	2.62
9-12	14.97	6.50	18.20	7.01	13.04	5.00
Notes						
* The value(s) in this column refer to which radial location(s) of the wake was set to the circumferential mean value.						
** Units (F)orce (thrust) - pounds; (T)orque - foot pounds						

Table 5. Calculated Total, Unsteady Thrust and Torque for Fin 3.

Wake* Mod	N=12		N=24		N=36	
	F **	T **	F	T	F	T
None	51.57	26.43	35.69	15.72	5.05	1.81
1	56.48	27.41	35.57	15.69	5.07	1.81
2	54.21	27.09	35.93	15.77	5.07	1.82
3	54.02	27.09	36.05	15.81	4.71	1.73
4	53.46	27.01	35.56	15.68	4.60	1.68
5	51.65	26.48	34.64	15.37	4.07	1.49
6	50.65	26.09	33.49	14.90	3.40	1.22
7	49.16	25.47	32.24	14.30	3.45	1.20
8	46.33	24.14	30.14	13.30	1.98	0.67
9	46.94	24.37	30.49	13.34	1.23	0.08
10	14.35	5.15	19.33	8.21	10.74	4.39
11	53.68	27.42	34.08	15.04	7.77	3.03
12	51.58	26.43	35.67	15.71	5.06	1.81
1-2	59.18	28.08	35.81	15.75	5.09	1.82
3-8	47.59	24.18	23.72	10.80	4.82	2.06
9-12	9.63	2.55	12.12	5.01	9.15	3.58
Notes						
* The value(s) in this column refer to which radial location(s) of the wake was set to the circumferential mean value.						
** Units (F)orce (thrust) - pounds; (T)orque - foot pounds						

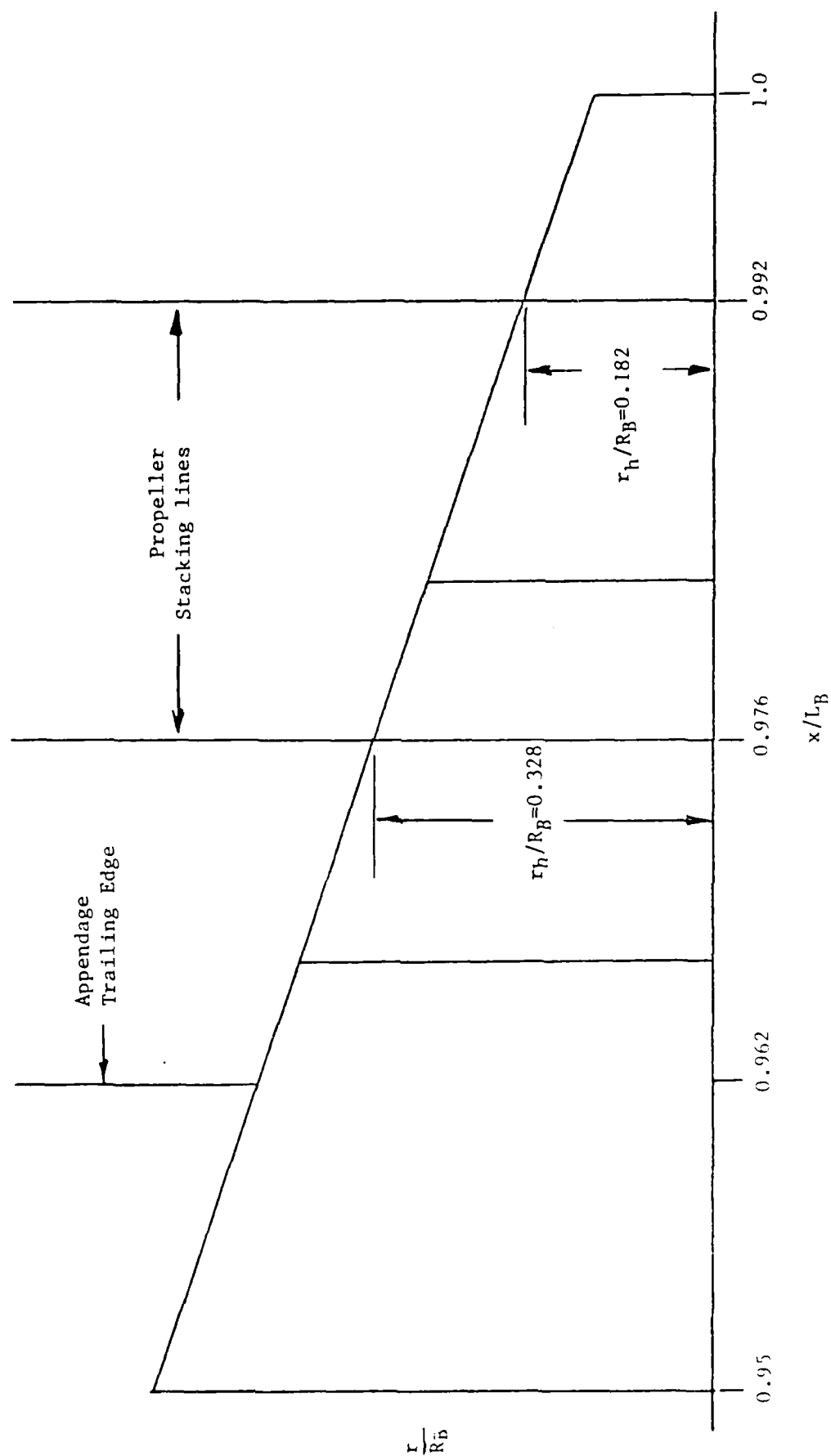


Figure 1. Sketch of the Afterbody Geometry.

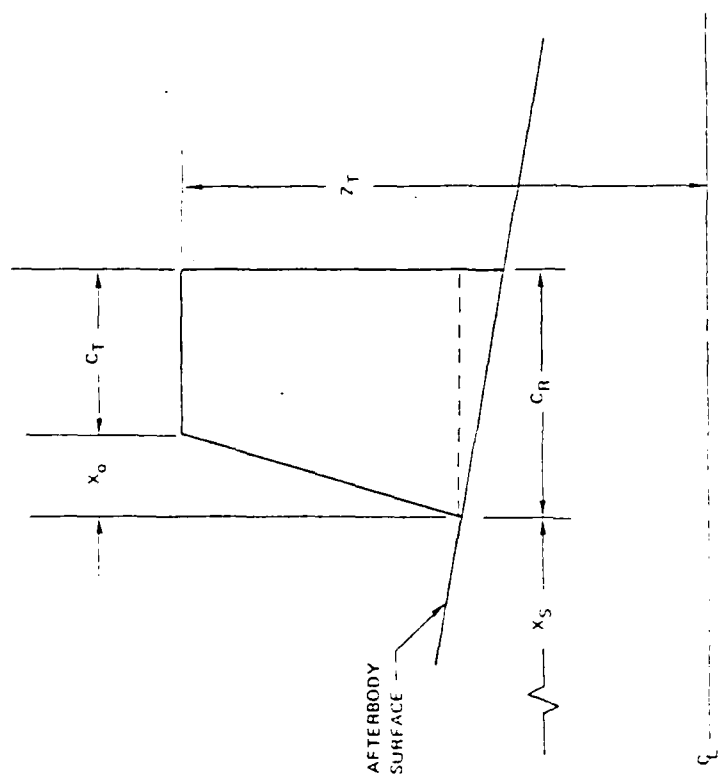
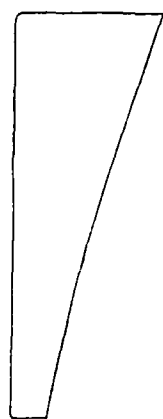
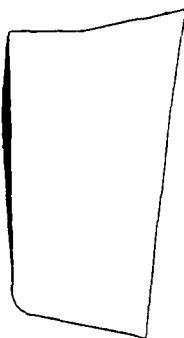


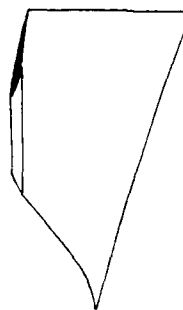
Figure 2 Definition of Appendage Geometry.



Fin 1



Fin 2



Fin 3

Figure 3 Sketch of the Appendage Configurations.

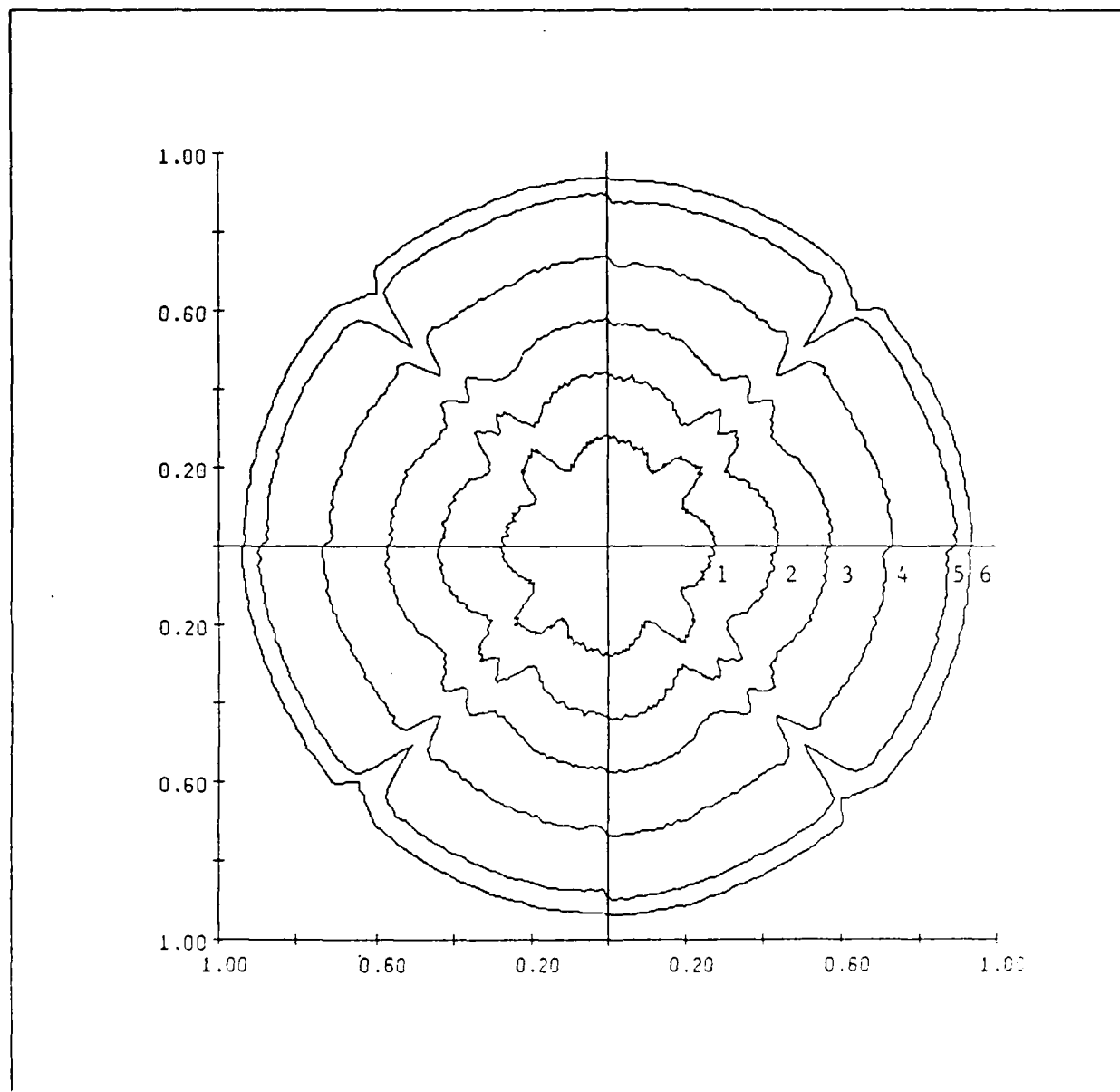


Figure 4. Circumferential Variation of the Measured Axial Inflow Velocity, V/V_s , (plotted radially), for various radial locations r/R_B and Fin 1. (Radial positions: 1-0.35; 2-0.41; 3-0.48; 4-0.60; 5-0.74; 6-0.90)

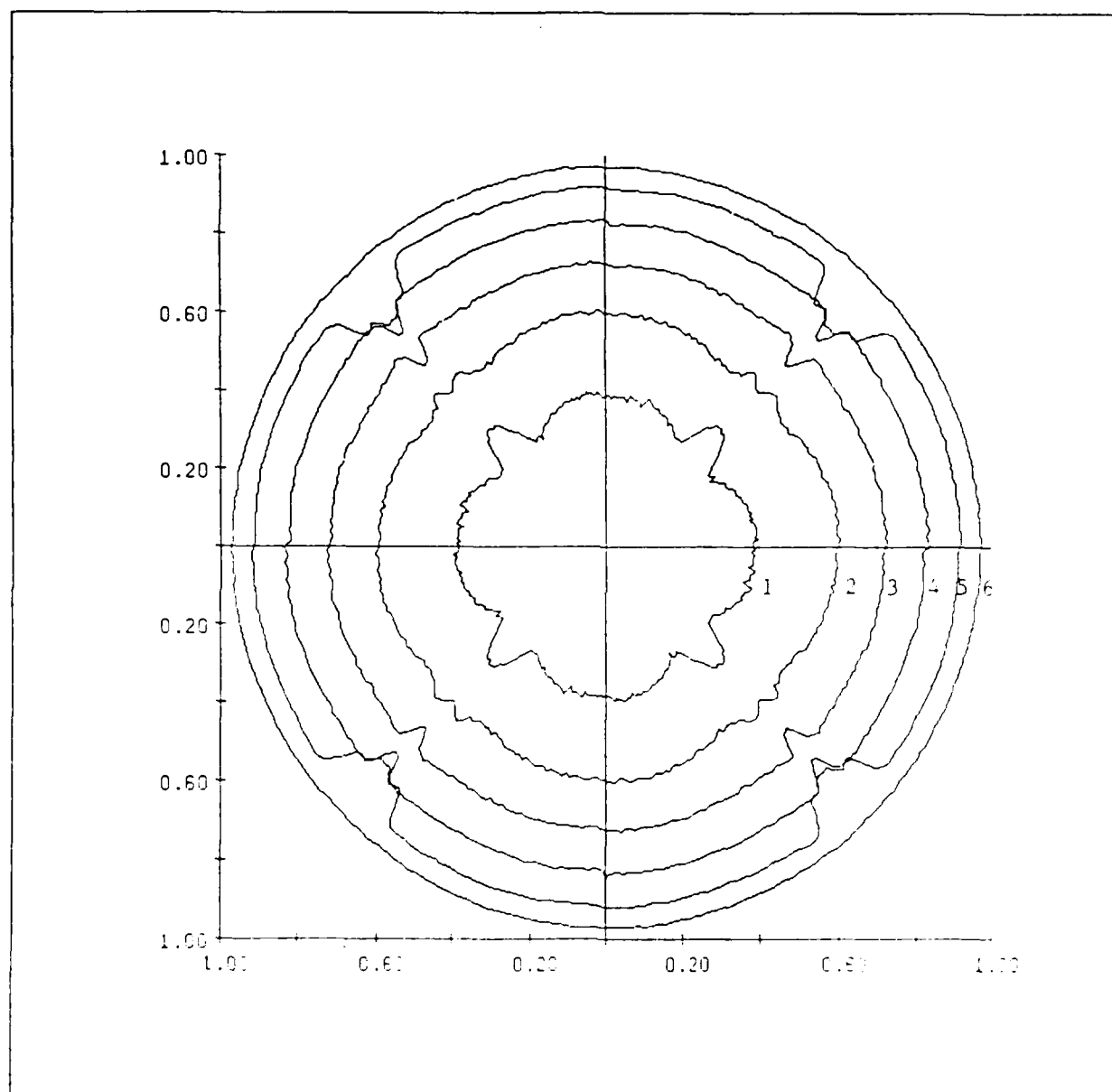


Figure 5. Circumferential Variation of the Measured Axial Inflow Velocity, V/V_0 , (plotted radially), for various radial locations r/R_B and Fin 2. (Radial positions: 1-0.35; 2-0.41; 3-0.48; 4-0.60; 5-0.74; 6-0.90)

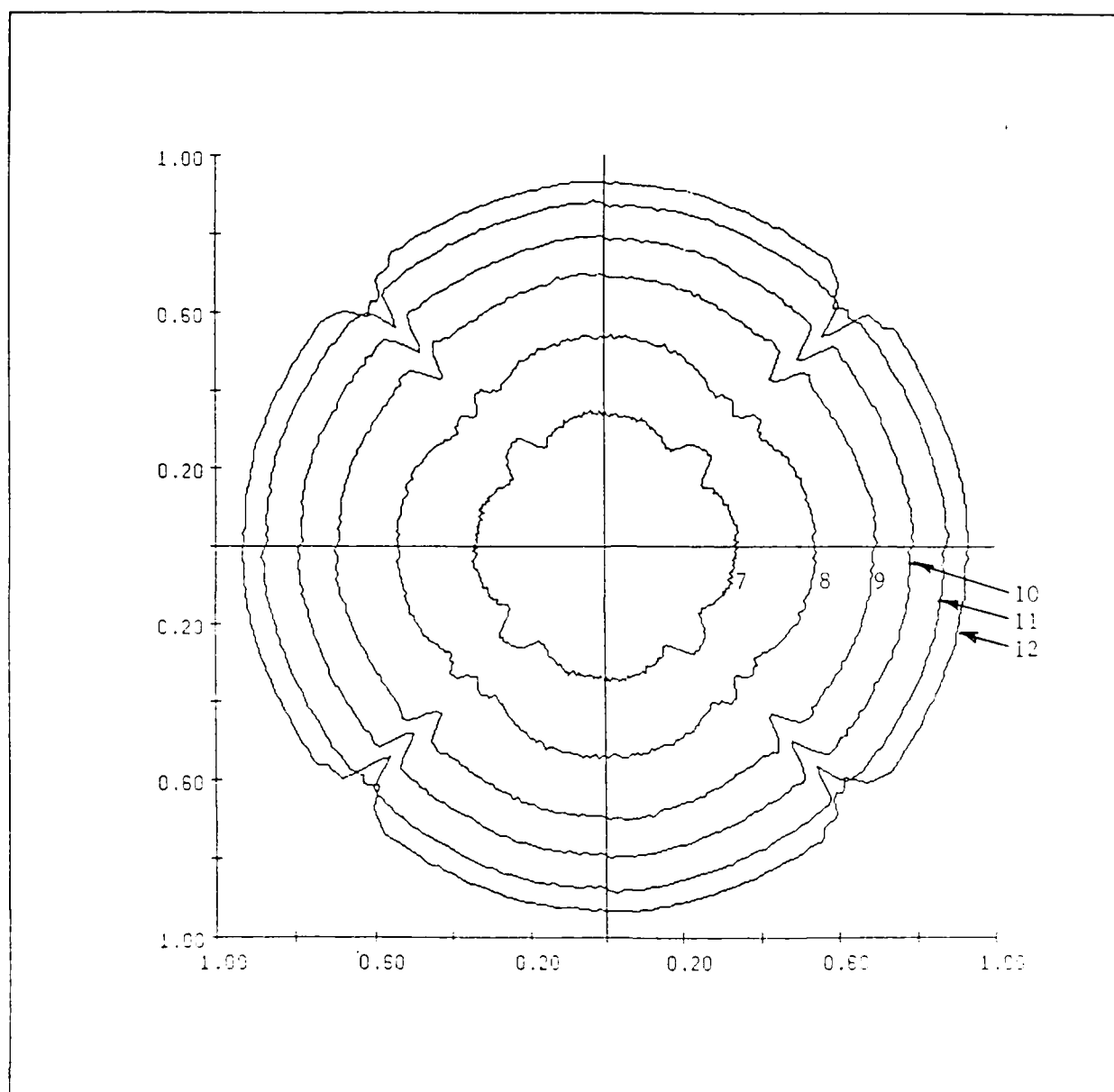


Figure 6. Circumferential Variation of the Measured Axial Inflow Velocity, V/V_0 , (plotted radially), for various radial locations r/R_0 and Fin 3. (Radial positions: 7-0.37; 8-0.44; 9-0.54; 10-0.68; 11-0.86; 12-1.05)

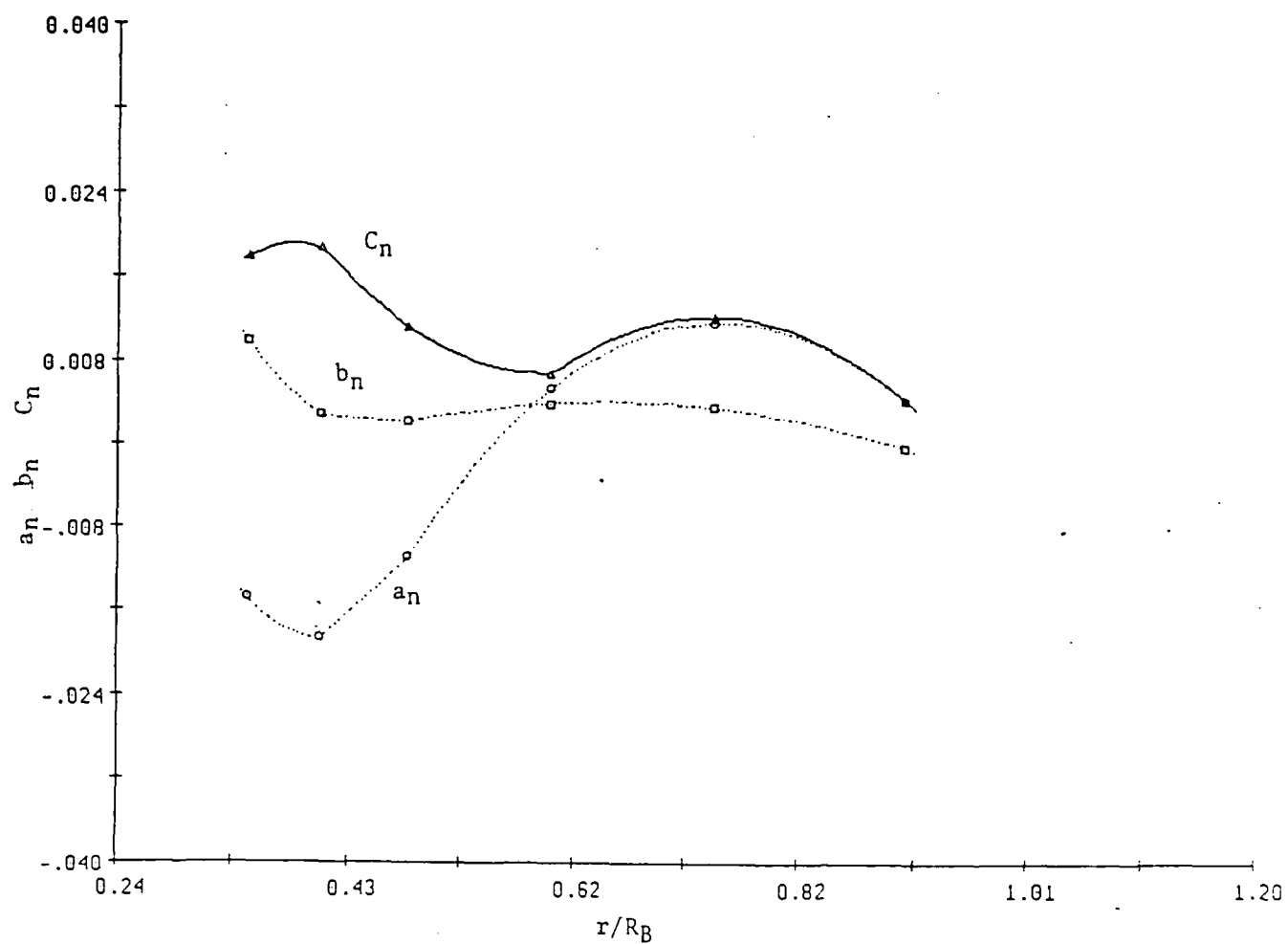


Figure 7. Variation of Fourier Coefficient Amplitude With Radial Position, r/R_B , for Harmonic Number $N=12$ and Fin 1.

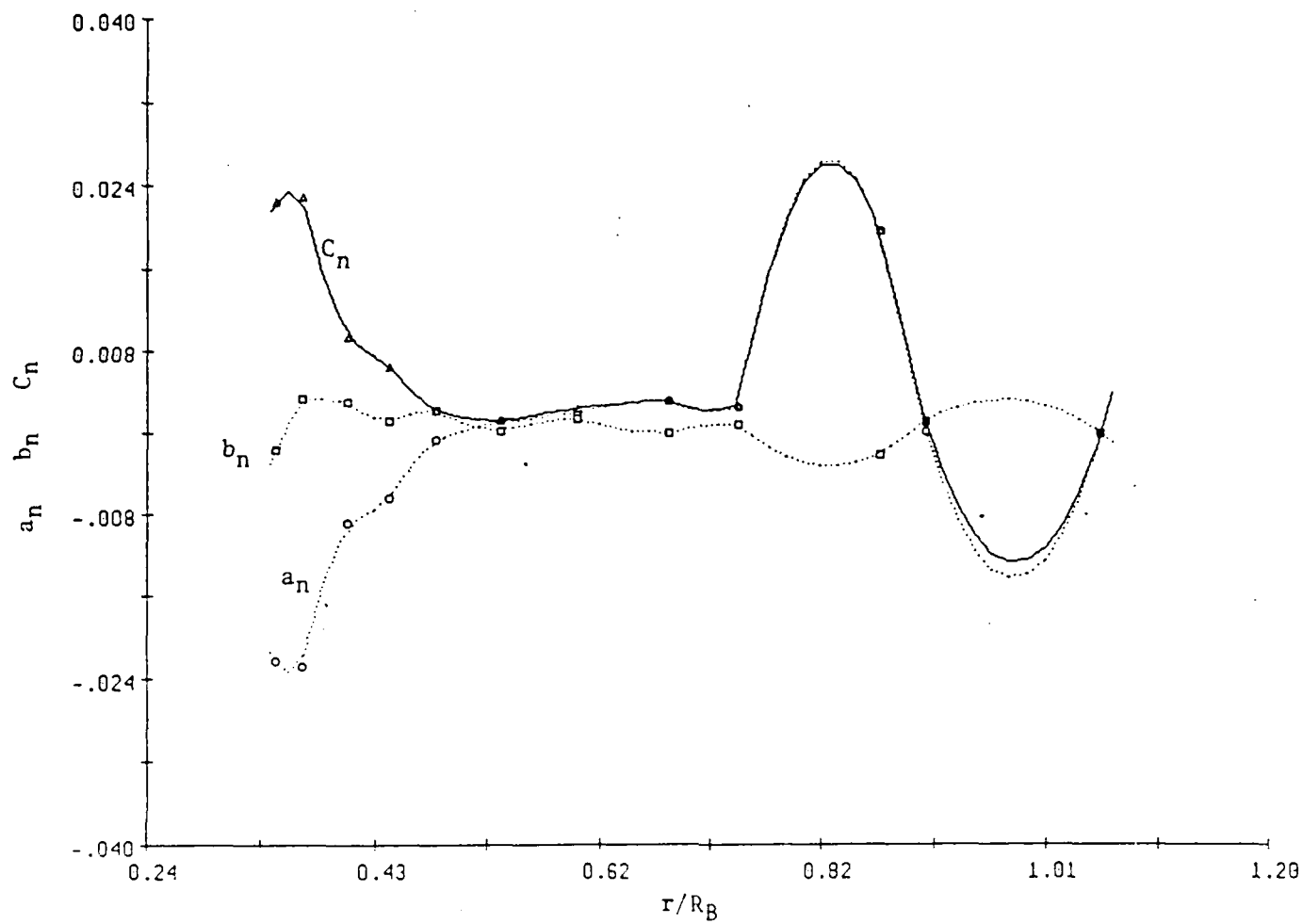


Figure 8. Variation of Fourier Coefficient Amplitude With Radial Position, r/R_B , for Harmonic Number $N=12$ and Fin 2.

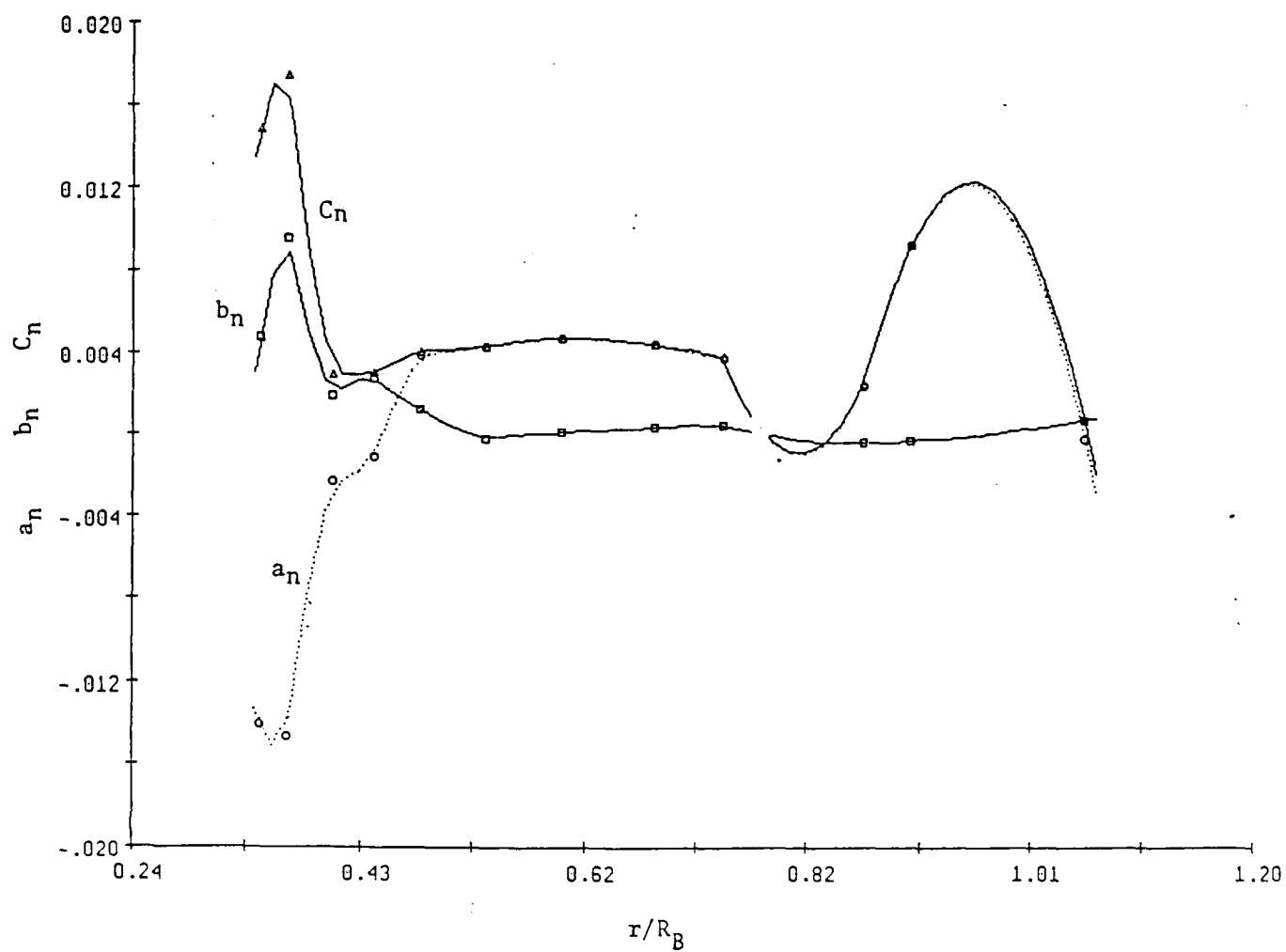


Figure 9. Variation of Fourier Coefficient Amplitude With Radial Position, r/R_B , for Harmonic Number $N=12$ and Fin 3.

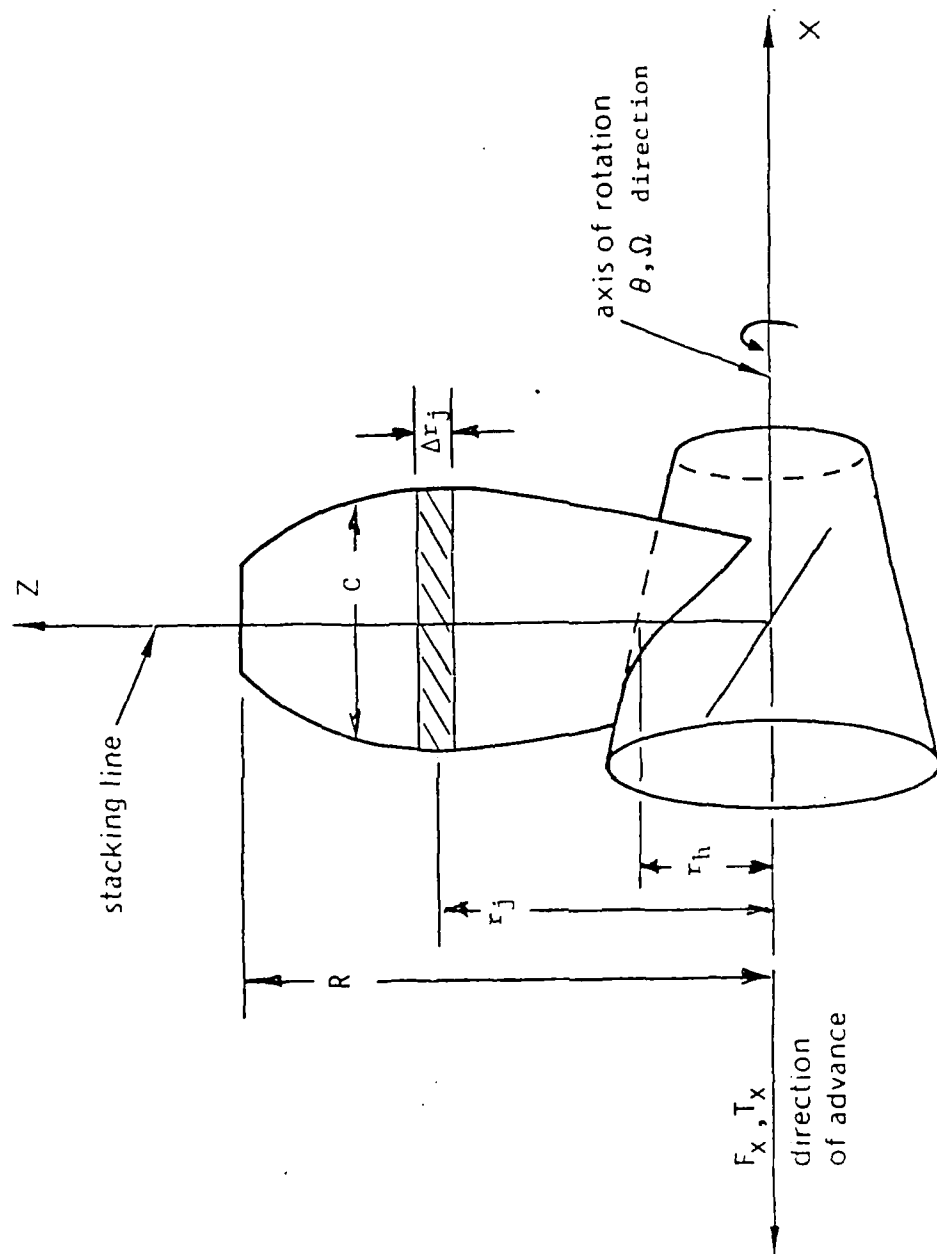


Figure 10. Description of a Typical Propeller and its Geometry

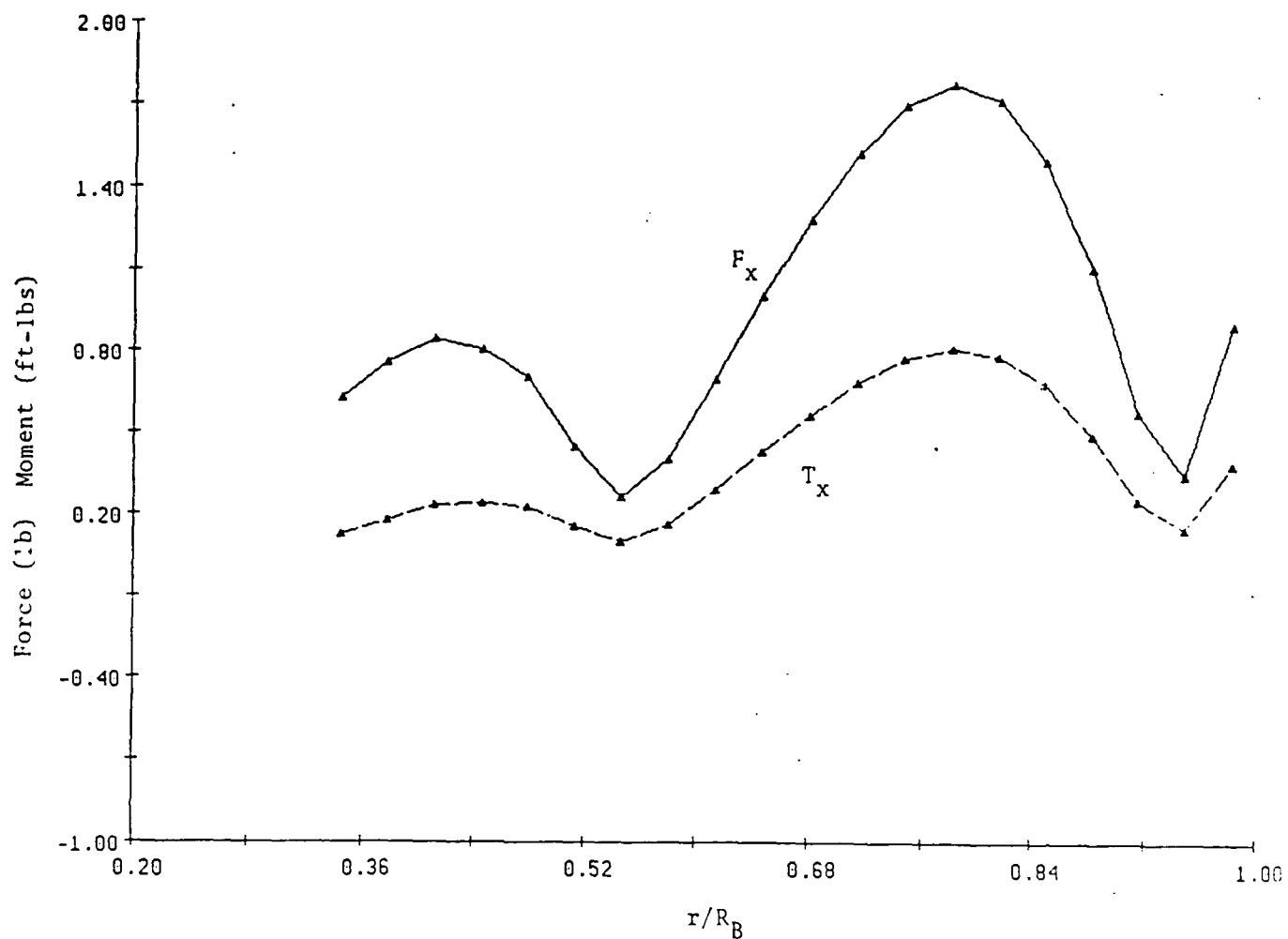


Figure 11. Variation of the Unsteady Thrust, F_x , and Torque, T_x , with Radial Position, r/R_B , for Harmonic Number $N=12$ Using Fin 1.

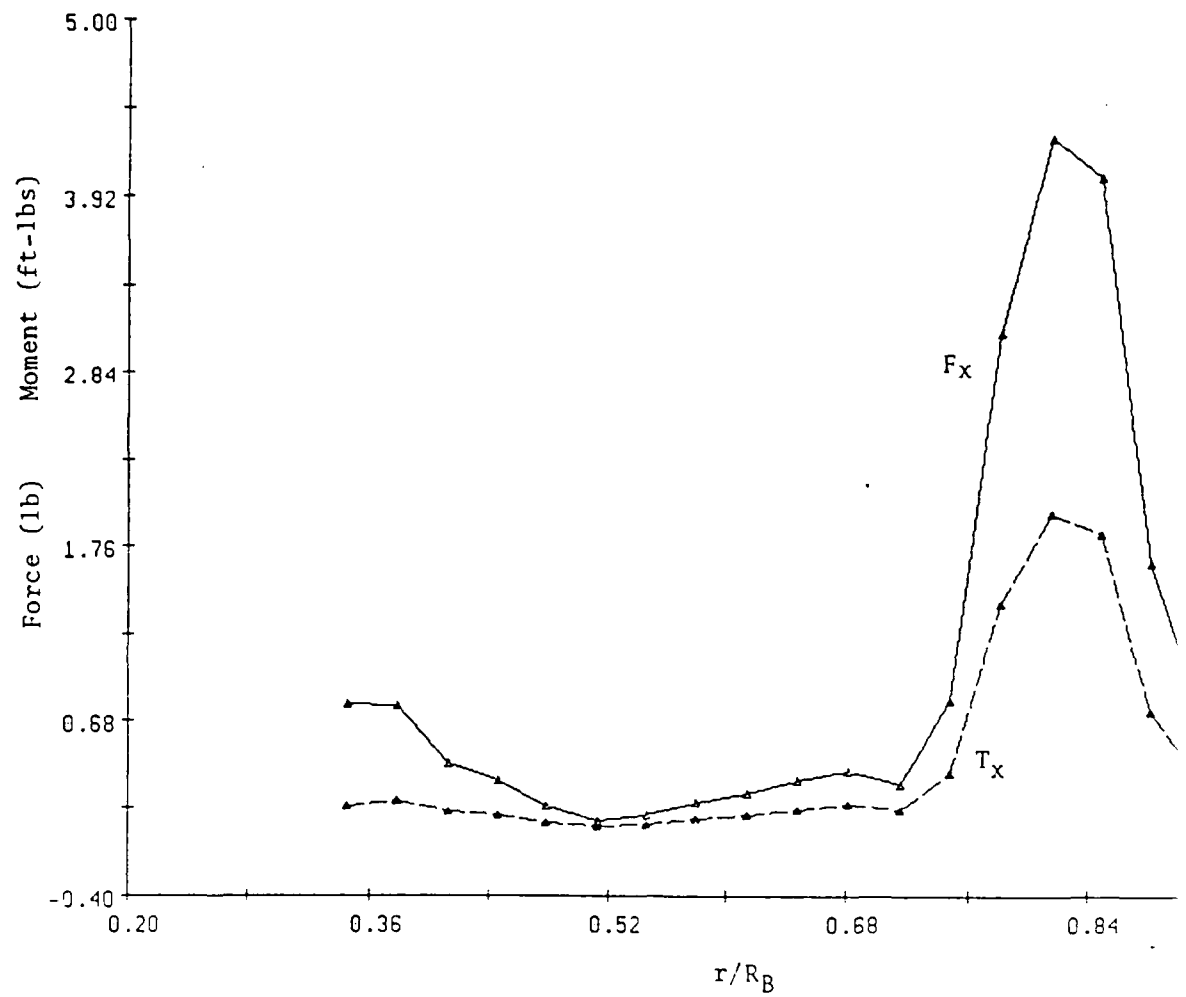


Figure 12. Variation of the Unsteady Thrust, F_x , and Torque, T_x , with Radial Position, r/R_B , for Harmonic Number $N=12$ Using Fin 2.

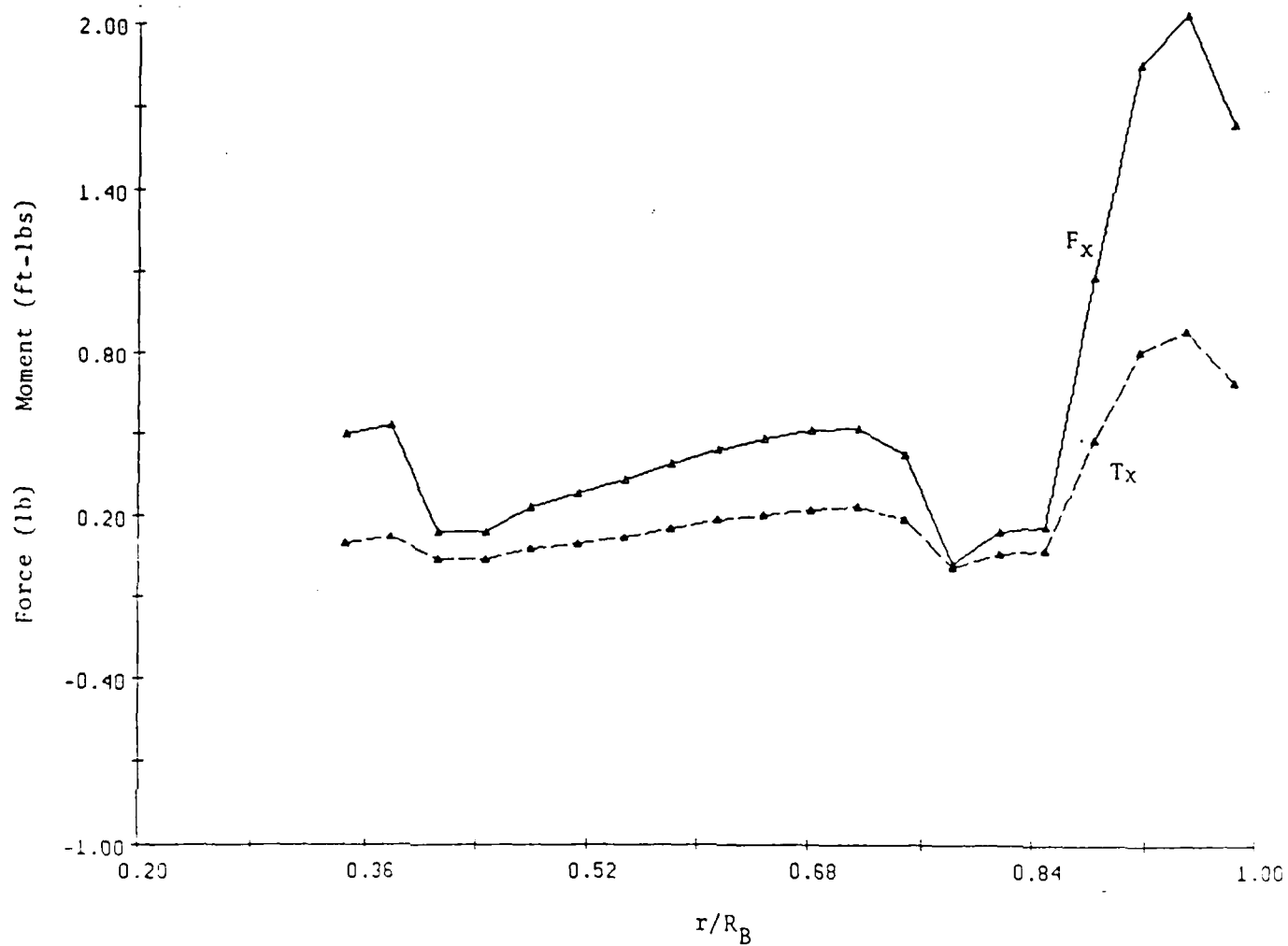


Figure 13. Variation of the Unsteady Thrust, F_x , and Torque, T_x , with Radial Position, r/R_B , for Harmonic Number $N=12$ Using Fin 3.

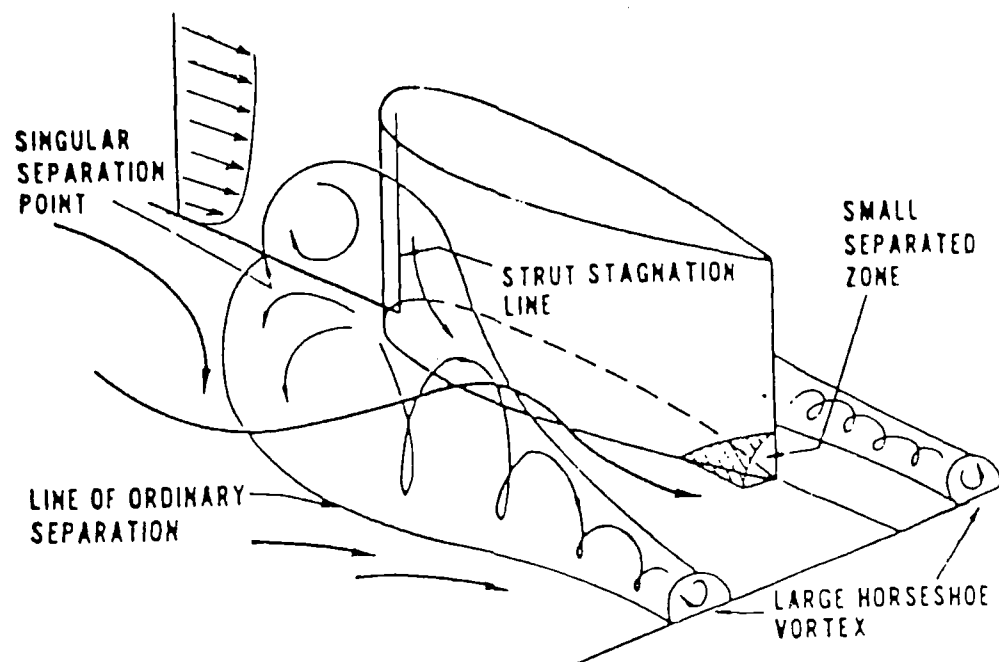


Figure 14. Model of the Thick Boundary Layer Appendage Interaction (from Barber, 1978).

END

DATE

FILMED

6-1988

DTIC